frontiers in Materials

ORIGINAL RESEARCH
published: 17 March 2022
doi: 10.3389/fmats.2022.843265

Enhanced Magneto-Optical Effect in Heterostructures Composed of Epsilon-Near-Zero Materials and Truncated Photonic Crystals

Shengyu Hu[1], *Zhiwei Guo*[1,2]*, *Lijuan Dong*[2], *Fusheng Deng*[2], *Haitao Jiang*[1]* *and Hong Chen*[1]

[1]Key Laboratory of Advanced Micro-Structure Materials, MOE, School of Physics Science and Engineering, Tongji University, Shanghai, China, [2]Shanxi Provincial Key Laboratory of Microstructure Electromagnetic Functional Materials, Shanxi Datong University, Datong, China

Optical non-reciprocal transmission plays an important role in many applications such as optical isolation, switching, and integrated photonic circuits. However, the non-reciprocity of natural magneto-optical (MO) materials is too weak to be widely used in the actual applications. Magnetized metamaterials enable the exploration of a new regime about the MO effect, including the enhanced non-reciprocal transmission and one-way surface waves. In this work, the Fano-type interference effect is studied in the heterostructure composed of a magnetized epsilon-near-zero material and a truncated photonic crystal. The inherent weak MO activity is significantly enhanced in the heterostructure because of the field intensity enhancement mechanism and Fano interference. The results provide a way to design novel optical non-reciprocal devices with excellent performance using metamaterials.

Keywords: photonic crystal, zero-index metamaterials, magneto-optical effect, Fano interference, high-Q mode

OPEN ACCESS

Edited by:
Xiao-Dong Chen,
Sun Yat-sen University, China

Reviewed by:
Cuicui Lu,
Beijing Institute of Technology, China
Wenguo Zhu,
Jinan University, China

***Correspondence:**
Haitao Jiang
jiang-haitao@tongji.edu.cn
Zhiwei Guo
2014guozhiwei@tongji.edu.cn

Specialty section:
This article was submitted to Metamaterials, a section of the journal Frontiers in Materials

Received: *25 December 2021*
Accepted: *28 February 2022*
Published: *17 March 2022*

Citation:
Hu S, Guo Z, Dong L, Deng F, Jiang H and Chen H (2022) Enhanced Magneto-Optical Effect in Heterostructures Composed of Epsilon-Near-Zero Materials and Truncated Photonic Crystals. Front. Mater. 9:843265. doi: 10.3389/fmats.2022.843265

INTRODUCTION

The non-reciprocal transmission phenomenon, which breaks the symmetry of time inversion, has attracted more and more attention recently. The magneto-optical (MO) effect provides a stable, ultrafast, and high-resolution optical control method, and the non-reciprocity revealed by the Onsager–Casimir principle has a wide range of applications (Kharratian et al., 2020), such as optical isolators (Takeda and John, 2008; Bi et al., 2011; Zhang et al., 2019), all-optical signal processing, circulators (Smigaj et al., 2010; Dmitriev et al., 2012; Pintus et al., 2013), and fast imaging (Zhang et al., 2018). Thus far, however, structures have usually exhibited a weak one-way transmission effect even under some judicious designs as the strength of MO activity of the natural materials is extremely small. Metamaterials, artificial materials composed of subwavelength unit cells, provide a powerful platform for manipulating the propagation of light (Liberal and Engheta, 2017; Niu et al., 2018; Guo et al., 2022). Leviyev et al. (2017) proposed that the one-way surface plasmon polaritons (SPPs) can be realized based on the MO hyperbolic metamaterials. In particular, the photonic crystals (PCs) containing the metamaterials have become the focus of scientific research because of their unique characteristics of enhancing light–matter interactions (Guan et al., 2006). Guo et al. (2018) uncovered the non-reciprocal transmission in the one-dimensional (1D) PCs with the magnetized epsilon-near-zero (ENZ) defect. Moreover, they showed that the wavelength difference of transmission peaks along two opposite incident directions can be significantly enhanced over two orders of magnitude compared with the bismuth iron garnet MO defect.

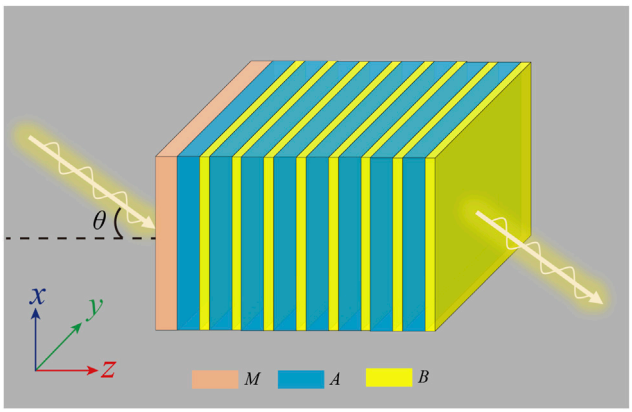

FIGURE 1 | Schematic of the heterostructure composed of a magnetized isotropic ENZ layer *M* and a truncated PC: $(AB)_n$. *M*, *A*, and *B* correspond to the Ag, SiO_2, and TiO_2, respectively. The incident electromagnetic waves launch into the structure from the left at an incident angle θ.

This large non-reciprocal effect does not resort to the enhancement of MO activity by the strong external magnetic field and opens novel routes to exploit advanced materials for steering the non-reciprocal transmission of electromagnetic waves in nano-scale structures (Sounas et al., 2013; Guo et al., 2018). We know that some special interference effects will significantly enhance the interaction between light and matter. Therefore, the interference effect combined with MO metamaterials and PCs is promising to further enhance the MO effect.

Fano interference is a ubiquitous scattering wave phenomenon, and it can describe the interaction of waves from quantum interference to classical physics (Fano, 1961; Miroshnichenko et al., 2010; Limonov et al., 2017). At present, Fano interference in classical systems has produced a series of interesting physical phenomena and applications, such as slow light effect (Wu et al., 2011), molecular recognition (Yanik et al., 2011; Wu et al., 2012), optical switching (Argyropoulos et al., 2012; Dabidian et al., 2015), sensing (Gupta et al., 2017), and coding (Manjappa et al., 2018). It is worth mentioning that Zhang et al. (2013) found that Fano interference can be used to significantly reduce the threshold value of optical switching and bistability. In addition, Singh et al. (2014) found new high-sensitivity sensors based on Fano interference, and the sensitivity even exceeds quadrupole resonance. Although Fano interference can be used to enhance the light–matter interaction, it is mainly realized by adjusting structural parameters (Vlasov et al., 2001; Rybin et al., 2009; Poddubny et al., 2012; Rybin et al., 2013; Pariente et al., 2016; Rybin et al., 2016; Tribelsky and Miroshnichenko, 2016). It is very meaningful to realize the Fano interference of active control (Ott et al., 2013).

In this work, aiming at the aforementioned problems, we study the Fano interference realized by heterostructures composed of ENZ material and truncated photonic crystals. In particular, we verify that the asymmetric transmittance profile of the heterostructure spectrum due to Fano-type interference can be flexibly tuned by controlling the direction of the external magnetic field. The MO enhancement properties of isotropic and anisotropic ENZ materials are similar. Therefore, our results not only reveal an actively controlled Fano interference using the external magnetic field but also demonstrate the field enhancement effect of the ENZ material, together with the asymmetric characteristic of the Fano-type transmission, can enhance the MO effect and realize non-reciprocal transmission. In addition to non-reciprocal transmission, the results of this study also provide new ways for bound states in the continuum (BIC) (Bogdanov et al., 2019; Tan et al., 2020) and topological state (Zangeneh-Nejad and Fleury, 2019) manipulation, which is expected to be used to construct new optical sensors (Guo et al., 2021a), lasers (Yu et al., 2021), and energy transfer devices (Pham et al., 2017; Guo et al., 2021b).

RESULTS AND DISCUSSION

We consider the structure, shown in **Figure 1**, which is composed of a magnetized isotropic epsilon-near-zero (ENZ) material layer *M* and a truncated PC: $(AB)_n$. In particular, *M*, *A*, and *B* correspond to the Ag, SiO_2, and TiO_2, respectively. The electromagnetic waves with transverse magnetic (TM) polarization (E_x, H_y, E_z) launch into the structure with an incident angle θ. We suppose that the external magnetic field is in the *y*-direction, and the permittivity of Ag can be written as follows (Yu et al., 2008; Tuz, 2016):

$$\overline{\varepsilon_M} = \begin{pmatrix} \varepsilon_{xx} & 0 & -i\alpha \\ 0 & \varepsilon_{yy} & 0 \\ i\alpha & 0 & \varepsilon_{zz} \end{pmatrix}, \tag{1}$$

where $\varepsilon_{xx} = \varepsilon_{yy} = \varepsilon_{zz} = \varepsilon_M = \varepsilon_\infty - \frac{\omega_p^2}{\omega(\omega+i\gamma)}$. α denotes the strength of MO coefficient of the medium. Here, ε_∞ is the high-frequency permittivity with a value of 4.09 for Ag. $\omega_P = (N_0 e^2/\varepsilon_0 m^*)^{\frac{1}{2}} = 1.33 \times 10^{16}\ rad/s$ is the plasma frequency, where N_0, e, and m^* are the free electron density, charge, and effective electron mass, respectively. In particular, the MO coefficient can be expressed by $\alpha = i\frac{\omega_B}{\omega}\frac{\omega_p^2}{(\omega+i\gamma)^2-\omega_B^2}$ (Yu et al., 2008; Leviyev et al., 2017). $\omega_B = eB/m^*$ denotes the cyclotron frequency, which is dependent on the external magnetic field B. The diagonal permittivity is not affected by the magnetic field. $\gamma = 1.13 \times 10^{14}$ is the damping frequency. For the wavelength, $\lambda_0 = 286.5$ nm, the permittivity of Ag is $\varepsilon_M \approx 0 + 0.06\,i$, which corresponds to the epsilon-near-zero (ENZ) media. The refractive index of the SiO_2 and TiO_2 are 1.46 and 2.56, respectively. Considering the TM wave impacting the structure with $\theta = 50^\circ$, the first bandgap of PC is determined by the Bragg condition $\phi = k_{Az}d_A + k_{Bz}d_B = \pi$, where k_{Az} and k_{Bz} are the wavevectors in the layer *A* and layer *B*, respectively. In order to obtain the definite Fano-type interference between the ENZ layer and the PC structure, the center of bandgap should be near the ENZ wavelength λ_0 of layer *M* (Manjappa et al., 2018). Here, the thickness of non-magnetic layers of *A* and *B* is set as $d_A = 70$ nm and $d_B = 25$ nm, respectively.

For the magnetized Ag layer in **Eq. 1**, the TM and transverse electric (TE) polarization are completely decoupled, and the EMs

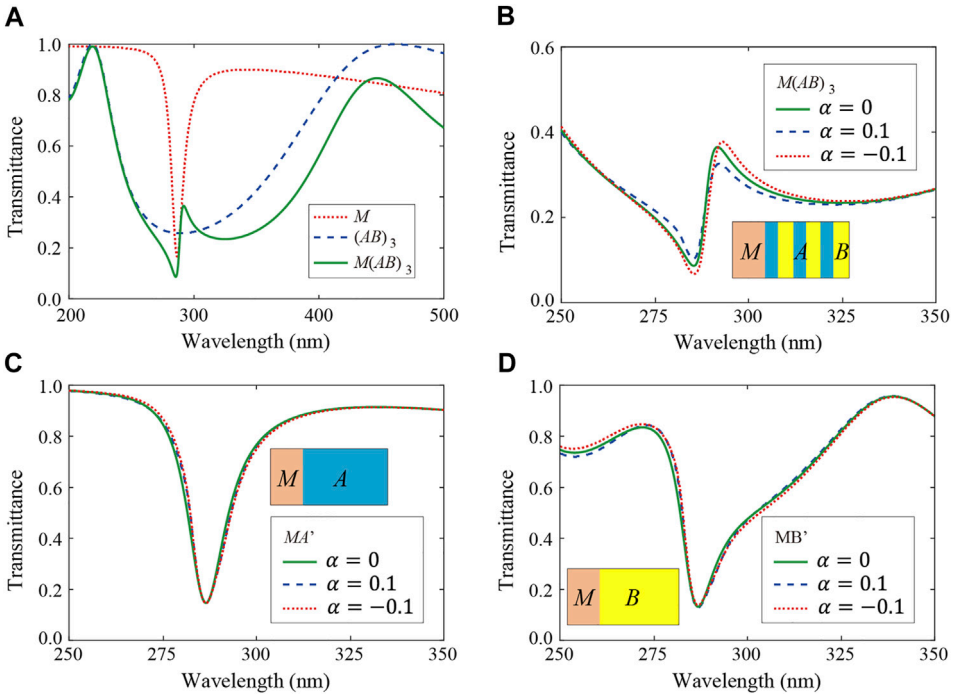

FIGURE 2 | (A) Transmittance spectrum of single *M* layer, the 1DPC: $(AB)_3$, and their composite structure $M(AB)_3$ without external magnetic field $\alpha = 0$, which corresponds to the dotted red line, dashed blue line, and solid green line, respectively. Here, $d_A = 70$ nm, $d_B = 25$ nm, $d_M = 10$ nm, and $\theta = 50^\circ$. **(B)** The transmittance spectrum of the composite structure $M(AB)_3$ for different MO coefficient: $\alpha = 0$ (solid green line), $\alpha = 0.1$ (dashed blue line), and $\alpha = -0.1$ (dotted red line), respectively. **(C, D)** Similar to **(B)**, but for the heterostructures *MA* and *MB*, respectively. The thickness of layer *A* in **(C)** [*B* in **(D)**] 285 nm, which is the same as the total thickness of 1DPC: $(AB)_3$ in **(B)**. Inset figures in **(B–D)** show the schematic of corresponding structures.

will maintain their initial polarization during propagation. As a result, the concise 2 × 2 transfer matrix method can be used to study the non-reciprocal transmission of the heterostructure in **Figure 1** (Guo et al., 2018). The incident angle of TM-polarized wave is selected to be $\theta = 50^\circ$. **Figure 2A** shows the transmittance spectrum of the single magnetized isotropic epsilon-near-zero material layer *M*, the 1DPC: $(AB)_3$, and their composite structure $M(AB)_3$, which are marked by the dotted red line, dashed blue line, and solid green line, respectively. It can be seen that the single *M* layer [1DPC: $(AB)_3$] exhibits a sharp transmission dip (a broad forbidden band) at 286.5 nm (from 218 to 416 nm). It should be noted that the imperfect bandgap here is caused by the small number of photonic crystal layers. In particular, the interference between the discrete and broadband reflection pathway leads to the asymmetric Fano-type spectrum for the heterostructure $M(AB)_3$. The transmission peak and dip at 285.4 and 291.7 nm can be clearly identified, respectively.

The sign of the MO coefficient α will flip when the magnetic field in the backward directions is applied. In particular, the transmittance spectrum of the composite structure $M(AB)_3$ for different MO coefficient: $\alpha = 0$ (solid green line), $\alpha = 0.1$ (dashed blue line), and $\alpha = -0.1$ (dotted red line) are respectively shown in **Figure 2B**. We can find that the non-reciprocal transmission is realized in this heterostructure $M(AB)_3$. Moreover, the transmittance peak at the high frequency is more sensitive to the direction of the applied magnetic field than the transmission dip at the low frequency. For comparison, the transmittance spectrum of the heterostructures *MA* and *MB* for different MO coefficient is shown in **Figures 2C,D**, respectively. The thickness of layer *A* in **Figure 2C** and layer *B* in **Figure 2D** is the same as the total thickness of $(AB)_3$ in **Figure 2B**. We see that the transmitted spectrum with different MO coefficients nearly overlaps. Therefore, although the magnetized ENZ can realize the enhancement of the field (Guo et al., 2018), the associated MO effect is not evident in the heterostructures *MA* and *MB* with simple resonance. Fano interference provides an effective way to enhance the MO effect in heterostructures composed of epsilon-near-zero materials and truncated photonic crystals, as shown in **Figure 2B**.

In order to realize the MO effect based on the Fano-type interference effect in the heterostructure composed of epsilon-near-zero materials and truncated photonic crystals, we further study the dependence of the transmittance spectrum of the heterostructure $M(AB)_3$ on the incident angle, the thickness of layer *M*, and the strength of MO coefficient α. When $d_M = 10$ nm, we can find that non-reciprocal transmission will become more evident as the angle increases, as shown in **Figures 3A–C**. In particular, the different MO coefficients: $\alpha = 0$, $\alpha = 0.1$, and $\alpha = -0.1$ are marked by the solid green line, dashed blue line, and dotted red line, respectively. Similarly, when we set the incident angle $\theta = 50^\circ$, the MO effect will be enhanced by changing the thickness of layer *M* from 10 to 30 nm, which is shown in **Figures**

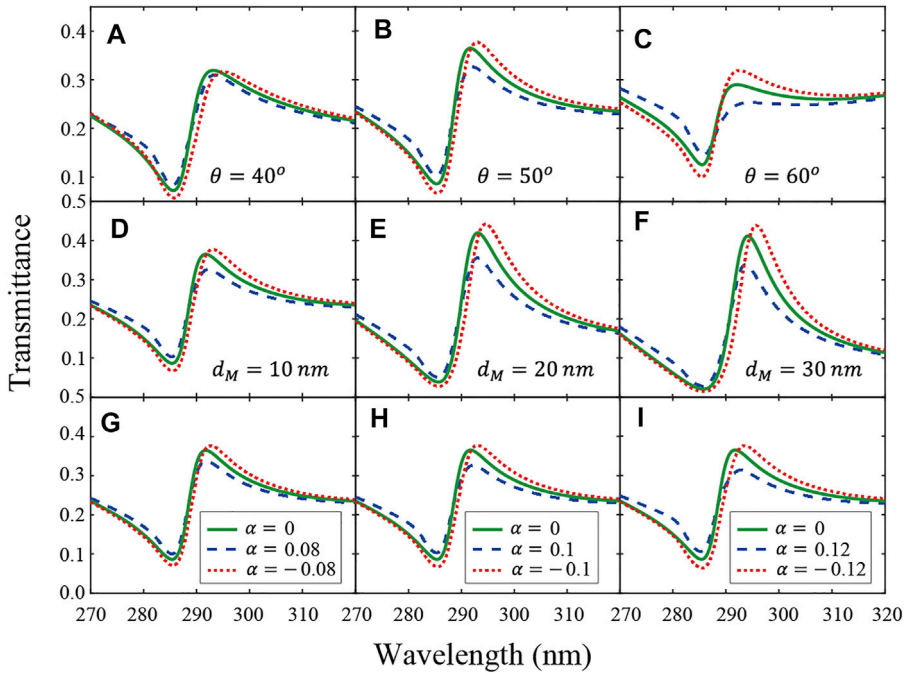

FIGURE 3 | (A)–(C) Transmittance spectrum of the composite structure $M(AB)_3$ for different incident angles: $\theta = 40^{\circ}$ **(A)**, $\theta = 50^{\circ}$ **(B)**, and $\theta = 60^{\circ}$ **(C)**. Solid green line, dashed blue line, and dotted red line denote the results for MO coefficient: $\alpha = 0$, $\alpha = 0.1$, and $\alpha = -0.1$, respectively. **(D–F)** Similar to **(A–C)**, but for the different thickness of layer M: $d_M = 10$ nm **(D)**, $d_M = 20$ nm **(E)**, and $d_M = 30$ nm, respectively. **(F)**. **(G–I)** Similar to **(A–C)**, but for the different strength of MO coefficient: $|\alpha| = 0.08$ **(G)**, $|\alpha| = 0.10$ **(H)**, and $|\alpha| = 0.12$ **(I)**, respectively.

TABLE 1 | Difference between the $\alpha > 0$ and $\alpha < 0$ at the transmission peak and transmission dip of the Fano-type spectrum.

	θ			dM			| α |		
	40°	50°	60°	10 nm	20 nm	30 nm	0.08	0.10	0.12
ΔT_d	0.027	0.036	0.045	0.036	0.023	0.014	0.030	0.036	0.043
ΔT_p	−0.007	−0.051	−0.066	−0.051	−0.087	−0.100	−0.039	−0.051	−0.062

3D–F. In addition, when we set the incident angle $\theta = 50^{\circ}$ and $d_M = 10$ nm at the same time, **Figures 3G–I** give the transmittance spectrum of the composite structure $M(AB)_3$ for the MO strength. It can be clearly seen that the MO effect will be significantly enhanced with the increase of MO strength. When the sign of optical coefficient α changes, due to the homogeneous property of Ag-based ENZ material, the transmittance dip of the Fano-type transmittance spectrum always appears at the zero point of permittivity of M layer. However, the transmittance peak will blueshift when α changes from negative to positive. In order to quantitatively analyze the dependence of MO effect on the aforementioned introduced different parameters, the difference between the $\alpha > 0$ and $\alpha < 0$ at the transmission peak and transmission dip of the Fano-type spectrum are denoted as ΔT_p and ΔT_d, respectively. ΔT_p and ΔT_d for different cases in **Figure 3** are summarized in **Table 1**.

Next, we study the dependence of MO effect on the incident angles, while the thickness of layer M and the strength of MO coefficient are fixed at $d_M = 10$ nm and $|\alpha| = 0.10$, respectively. In particular, in order to determine the difference of transmission on the MO coefficient, $\Delta T_1 = T|_{\alpha=0.1} - T|_{\alpha=0}$ and $\Delta T_2 = T|_{\alpha=0.1} - T|_{\alpha=-0.1}$ as a function of the wavelength and the incident angle are shown in **Figures 4A,B**, respectively. Here, the forward (backward) incident TM-polarized waves are denoted by $\theta > 0$ ($\theta < 0$). From **Figure 4A**, it can be seen that the transmittance will be strongly modified after applying the external magnetic field in this heterostructure with magnetized ENZ material. Moreover, the transmittance difference between two magnetic field directions ΔT_2 is studied, and the corresponding enhancement of the MO effect on the incident angle can be determined in **Figure 4B**. It can be seen that the forward incident ΔT_2 is opposite to the backward incident ΔT_2 (i.e., $\Delta T_2(\theta)$ is equal to $\Delta T_2(-\theta)$). The dashed line denotes the position of $\theta = 0^{\circ}$. The maximum of $|\Delta T_2|$ is marked by the white crosses, which are marked by the white crosses at $\theta = \pm 58^{\circ}$ and $\theta = \pm 67^{\circ}$, respectively.

The Fano profile of the heterostructure $M(AB)_3$ with magnetized ENZ material can also be flexibly controlled by

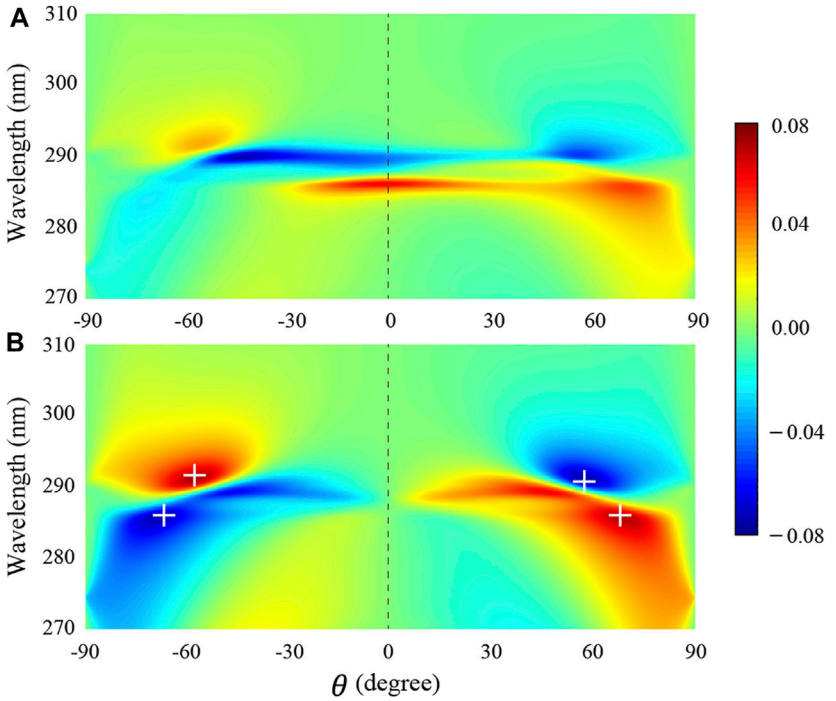

FIGURE 4 | (A) Dependence of $\Delta T_1 = T|_{\alpha=0.1} - T|_{\alpha=0}$ on the incident angle θ and wavelength when a TM-polarized plane wave is incident on the composite structure $M(AB)_3$. The dashed line denotes the position of $\theta = 0^\circ$. **(B)** Similar to **(A)**, but for the case of $\Delta T_2 = T|_{\alpha=0.1} - T|_{\alpha=-0.1}$. The maximum of $|\Delta T_2|$ is marked by the white crosses.

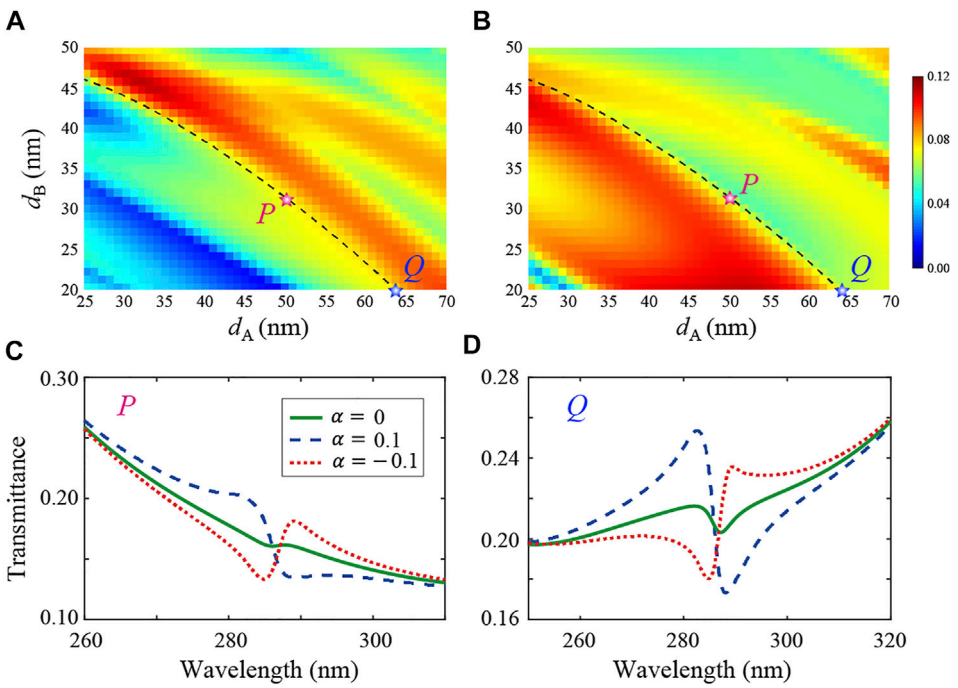

FIGURE 5 | (A) Maximum of ΔT_2 as the function of the thickness of layer *A* and layer *B*. **(B)** Similar to **(A)**, but for the maximum of $-\Delta T_2$. The places where Fano line changes sharply are distinguished by dashed lines. The case d_A = 50 nm (63 nm) and d_B = 32 nm (20 nm) is marked by *P* (*Q*). **(C)** The transmittance spectrum of the composite structure *P* for different MO coefficient: $\alpha = 0$ (solid green line), $\alpha = 0.1$ (dashed blue line) and $\alpha = -0.1$ (dotted red line), respectively. **(D)** Similar to **(C)**, but for the composite structure *Q*.

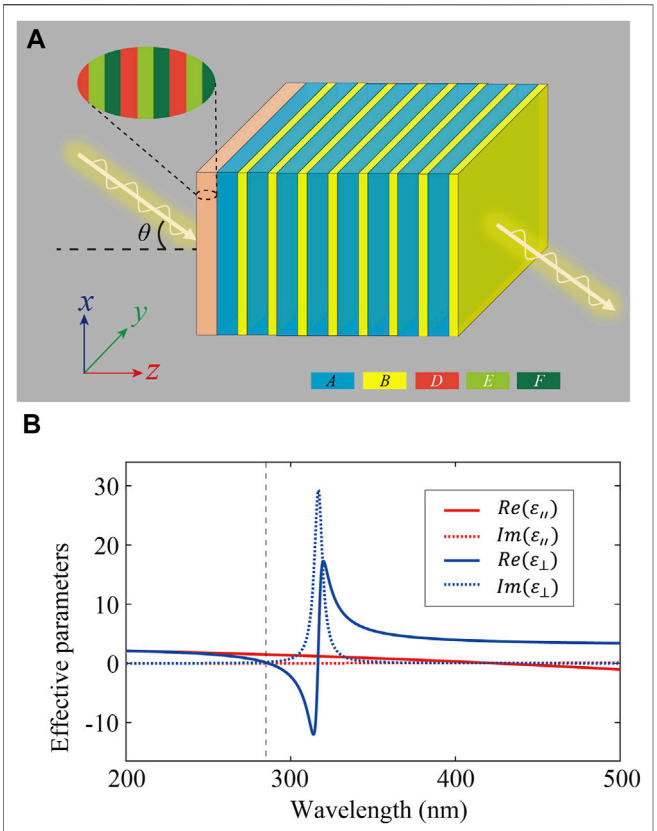

FIGURE 6 | (A) Schematic of the heterostructure composed of an effective magnetized anisotropic ENZ material layer $(DEF)_m$ and a truncated PC: $(AB)_n$. *D* and *F* correspond to the SiO_2 layer with the thickness of 5 and 2 nm, respectively. *E* denotes the Ag layer with the thickness of 3 nm. The incident electromagnetic waves launch into the structure from the left at an incident angle θ. **(B)** Effective anisotropic electromagnetic parameters based on the SiO_2/Ag/SiO_2 multilayer structure. $\varepsilon_{//}$ and $\varepsilon_{\perp}$ are marked by blue and red, respectively. The real part and imaginary part of the permittivity are shown by the solid line and dotted line, respectively. The magnetized anisotropic ENZ with negligible loss is marked by the black dashed line.

changing the external magnetic field. **Figures 5A,B** show the maximum of ΔT_2 and - ΔT_2 as the function of the thickness of layer *A* and layer *B* for different incident angles and wavelengths. The dashed lines denote the sensitivity of the heterostructure on the structure parameters that the maximum of ΔT_2 and - ΔT_2 are very close. We take two cases *P* and *Q* for example, which are marked by pink and blue stars, respectively. The variation of the direction of magnetic field can lead to different Fano asymmetric parameters and different asymmetry Fano resonance spectra, as shown in **Figures 5C,D** For the heterostructure *P* with d_A = 50 nm and d_B = 32 nm in **Figure 5C**, the Fano asymmetry parameter of the weak Fano-type spectrum is positive without the external magnetic field, as shown by the solid green line. After considering the positive magnetic field α >0, the Fano-type spectrum becomes clear (marked by the red dashed line) and the Fano asymmetry parameter is still positive because of the transmittance dip and peak appearing at low and high frequencies, respectively. However, when the magnetic field changes to negative α <0, the Fano asymmetry parameter is still negative because the transmittance dip and peak appear respectively at high and low frequencies. A similar property is demonstrated for the heterostructure *Q* with d_A = 63 nm and d_B = 20 nm, as shown in **Figure 5D**. Therefore, we can clearly see that the asymmetric transmittance profile of the heterostructure spectrum due to Fano-type interference can be flexibly tuned by controlling the direction of the external magnetic field. In addition, the behavior of enhanced magneto-optical activity for a TM wave in ENZ media is also suitable for an incident TE wave in mu-near-zero (MNZ) configuration.

The Fano-type interference effect in heterostructures actually exists in both isotropic and anisotropic ENZ components, regardless of the effective electromagnetic parameters. The heterostructures $C(AB)_n$ composed of an effective anisotropic magnetized ENZ layer and a truncated PC are studied. Similar to **Figure 1**, the schematic of the heterostructure with the effective anisotropic ENZ layer is shown in **Figure 6A**. Here the anisotropic ENZ layer is mimicked by subwavelength SiO_2/Ag/SiO_2 stacks as $(DEF)_M$. The unit cell of SiO_2/Ag/SiO_2 ensures that Ag is always clamped by SiO2, and the SiO2 layer plays a role in protecting the Ag layer. The thickness of the layers *D, E*, and *F* are 5 nm, 3, and 2 nm, respectively. Because the thickness of unit cell $d = d_D + d_E + d_F$ is far less than the wavelength of electromagnetic wave in the structure, the structure $(DEF)_M$ can be homogenized based on the effective medium theory (EMT) (Guo et al., 2022):

$$\varepsilon_{xx} = \varepsilon_{yy} = \varepsilon_{//} = \varepsilon_D f_D + \varepsilon_E f_E + \varepsilon_F f_F, \quad (2)$$

$$\varepsilon_{zz} = \varepsilon_{\perp} = \left(\varepsilon_D / f_D + \varepsilon_E / f_E + \varepsilon_F / f_F\right)^{-1}, \quad (3)$$

where $f_i = d_i/d$, $(i = D, E, F)$ denotes the filling ratio of component layer of anisotropic ENZ material. Based on **Eqs 2, 3**, the effective permittivity of the C layer is shown in **Figure 6B**. The complex $\varepsilon_{//}$ and $\varepsilon_{\perp}$ are marked by blue and red, respectively. The real part and imaginary part of the permittivity are shown by the solid line and dotted line, respectively. The magnetized anisotropic ENZ with negligible loss is marked by the black dashed line. In addition, to ensure consistency, the truncated PC $(AB)_n$ is the same as introduced before.

Here the enhanced MO effect by Fano interference is studied based on the narrow discrete resonance of the effective anisotropic ENZ layer and the broadband reflection of the truncated PC, as shown in **Figure 7A**. The incident angle is set as $\theta = 50^{\circ}$. Similar to **Figure 2A**, the constructive and destructive interference of the Fano-type spectrum is given based on the single *C* layer and the truncated PC (The transfer matrix of the effective anisotropic MO ENZ material can be found in the **Supplementary Material**). It can be seen that for the effective anisotropic ENZ layer, the transmittance spectrum exhibits a sharp transmission dip at 286 nm, which corresponds to a narrow discrete resonance, as shown by the dashed line in **Figure 7A**. Although EMT will become more effective with the increase of the number of unit cells, in the actual structure, we use limited unit cells $m = 3$ to illustrate the applicability of EMT. The transmittance spectrum of the $(DEF)_3$ is marked by the red dotted line, which met well with the results of effective single *C* layer. In addition, the

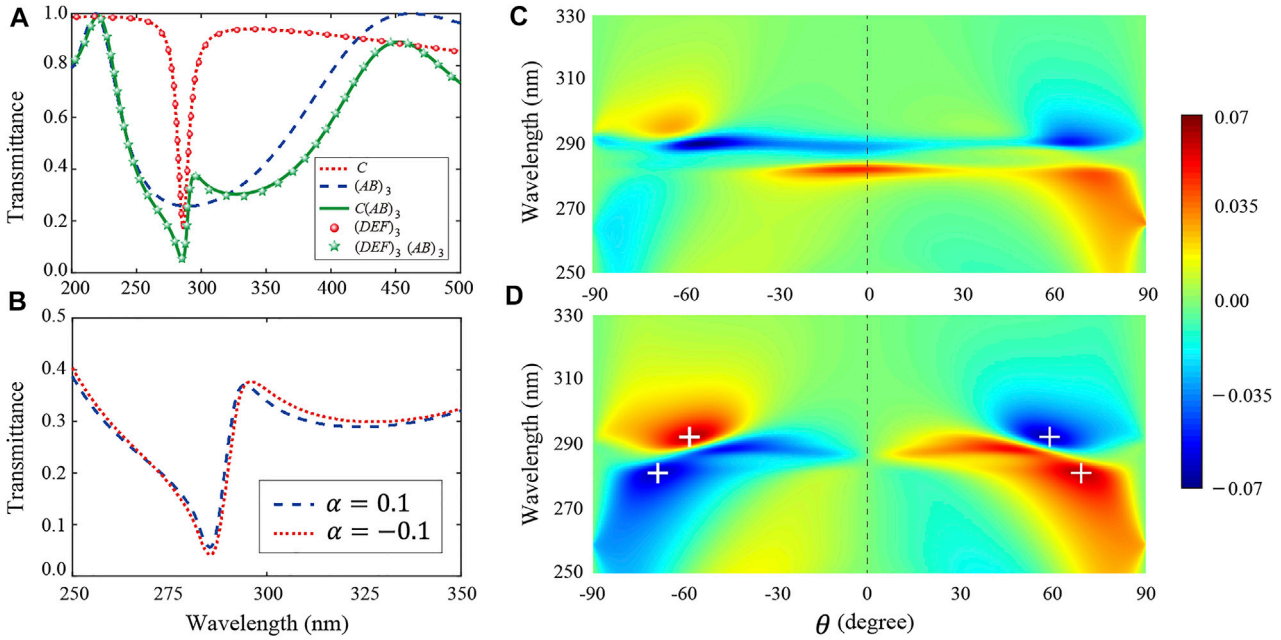

FIGURE 7 | (A) Transmittance spectrum of C layer based on the effective parameters from $(DEF)_m$, the 1DPC: $(AB)_3$, the composite structure: $C(AB)_3$, the multilayer structure: $(DEF)_3$, and the composite structure: $(DEF)_3(AB)_3$, which corresponds to the dotted red line, dashed blue line, solid green line, red dotted line, and green star line, respectively. The incident angle is $\theta = 50^\circ$. **(B)** The transmittance spectrum of the composite structure $(DEF)_3(AB)_3$ for different external magnetic field: $\alpha = 0.1$ (dashed blue line) and $\alpha = -0.1$ (dotted red line), respectively. **(C)** The dependence of $\Delta T_1 = T|_{\alpha=0.1} - T|_{\alpha=0}$ on the incident angle θ and wavelength when a TM-polarized plane wave is incident on the composite structure $(DEF)_3(AB)_3$. The dashed line denotes the position of $\theta = 0^\circ$. **(D)** Similar to **(C)**, but for the case of $\Delta T_2 = T|_{\alpha=0.1} - T|_{\alpha=-0.1}$. The maximum of $|\Delta T_2|$ is marked by the white crosses.

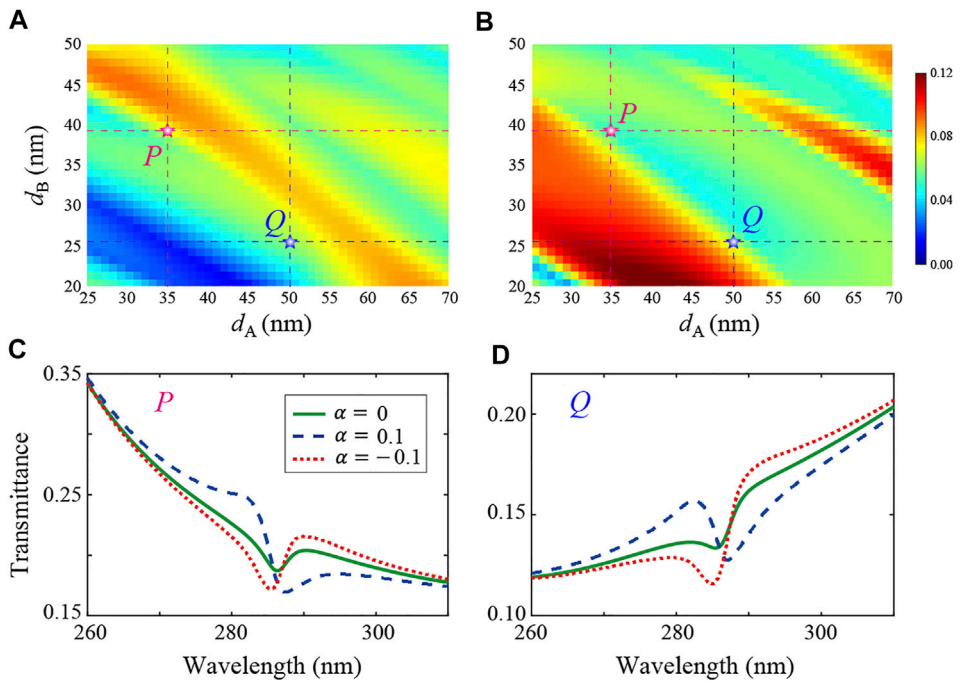

FIGURE 8 | (A) Maximum of ΔT_2 as a function of the thickness of layer *A* and layer *B*. **(B)** Similar to **(A)**, but for the maximum of $-\Delta T_2$. The places where Fano line changes sharply are distinguished by dashed lines. The case $d_A = 35$ nm (50 nm) and $d_B = 39$ nm (26 nm) is marked by *P* (*Q*). **(C)** The transmittance spectrum of the composite structure *P* for different MO coefficient: $\alpha = 0$ (solid green line), $\alpha = 0.1$ (dashed blue line) and $\alpha = -0.1$ (dotted red line), respectively. **(D)** Similar to **(C)**, but for the composite structure *Q*.

transmittance spectrum of the truncated PC $(AB)_3$ is given by the blue dashed line, which exhibits a broadband reflection from 218 to 416 nm. As a result, the interference between the discrete and broadband reflection pathway leads to the asymmetric Fano-type spectrum for the heterostructure. The transmission peak and dip at 285.4 and 295.1 nm can be clearly identified, respectively. The transmission spectrum of $C(AB)_3$ and $(DEF)_3(AB)_3$ nearly overlaps which further confirms the applicability of EMT. In particular, the transmittance spectrum of the composite structure $C(AB)_3$ for different MO coefficient $\alpha = 0.1$ and $\alpha = -0.1$ are shown in **Figure 7B**, which are marked by the dashed blue line and dotted red line respectively. Similar to the isotropic case, the transmittance peak at the high frequency of the heterostructure $C(AB)_3$ with anisotropic magnetized ENZ material is more sensitive to the transmission dip at the low frequency after changing the direction of the applied magnetic field. The dependence of $\Delta T_1 = T|_{\alpha=0.1} - T|_{\alpha=0}$ and $\Delta T_2 = T|_{\alpha=0.1} - T|_{\alpha=-0.1}$ on the wavelength and the incident angle are also shown in **Figures 7C,D**, respectively. The maximum of $|\Delta T_2|$ is marked by the white crosses in **Figure 7D**, which are marked by the white crosses at $\theta = \pm 57^{\circ}$ and $\theta = \pm 69^{\circ}$, respectively. The dependence of the transmittance spectrum of the heterostructure $C(AB)_3$ on different parameters (i.e., the incident angle, the thickness of MO layer, and the strength of MO coefficient) is also systematically studied (The dependence of transmittance spectrum of the anisotropic MO ENZ material on different parameters can be found in the **Supplementary Material**).

From the maximum of ΔT_2 and - ΔT_2 as the function of the thickness of layer A and layer B in **Figures 8A,B**, we take two cases P and Q to demonstrate the external magnetic field-controlled Fano profile based on the effective anisotropic ENZ material. The heterostructure at P with $d_A = 35$ nm and $d_B = 39$ nm and at Q with $d_A = 50$ nm and $d_B = 26$ nm are marked by pink and blue stars, respectively. The variation of the direction of magnetic field can lead to different Fano asymmetric parameters and different asymmetry Fano resonance spectra, as shown in **Figures 8C,D**. The transmittance spectrum for $\alpha = 0$, $\alpha = 0.1$, and $\alpha = -0.1$ is marked by the solid green line, dashed blue line, and dotted red line, respectively. Similar to the isotropic case in **Figure 5**, the external magnetic field-controlled asymmetric transmittance profile of the heterostructure spectrum is demonstrated in the heterostructure with effective magnetized anisotropic ENZ material in **Figures 8C,D**. At last, it should be noted that although the Fano interference can enhance the MO effect, the loss around the Fano interference dip is large, which may limit the application of the research results in some specific scenarios.

CONCLUSION

In summary, we investigated the Fano-type interference effect in the heterostructure composed of a homogenous isotropic (or an effective anisotropic) magnetized ENZ material layer and a truncated dielectric photonic crystal. The ENZ material provides a narrow reflection pathway, and the photonic crystal provides a broadband reflection pathway, which gives rise to the asymmetric Fano-type spectrum. By means of the field intensity enhancement of ENZ material and the Fano interference of the heterostructure, the enhanced MO activity is demonstrated from the non-reciprocal transmission spectrum. In particular, the MO effect which depends on the incident angle, the thickness of MO layer, and the MO coefficient is studied. Moreover, the asymmetric transmittance profile of the heterostructure spectrum can be flexibly tuned by controlling the direction of the external magnetic field. These results provide a new perspective to design novel magneto-optical devices with coherence mechanisms, such as optical isolators, high-sensitivity sensors, and switches.

DATA AVAILABILITY STATEMENT

The original contributions presented in the study are included in the article/**Supplementary Material**; further inquiries can be directed to the corresponding authors.

AUTHOR CONTRIBUTIONS

ZG and HJ put forward the initial idea and supervised the project. ZG and SH performed the theoretical calculations and wrote the manuscript. LD, FD, HJ, and HC helped with the theoretical analyses. All the authors contributed fully to the research. ZG and SH contributed equally to this work.

FUNDING

This work was supported by the National Key R&D Program of China (Grant No. 2016YFA0301101), the National Natural Science Foundation of China (NSFC) (Grant Nos. 12004284, 11774261, and 61621001), the Shanghai Science and Technology Committee (Grant No. 18JC1410900), the China Postdoctoral Science Foundation (Grant Nos. 2019TQ0232 and 2019M661605), the Fundamental Research Funds for the Central Universities (Grant No. 22120210579), and the Shanghai Super Postdoctoral Incentive Program.

SUPPLEMENTARY MATERIAL

The Supplementary Material for this article can be found online at: https://www.frontiersin.org/articles/10.3389/fmats.2022.843265/full#supplementary-material

REFERENCES

Argyropoulos, C., Chen, P.-Y., Monticone, F., D'Aguanno, G., and Alù, A. (2012). Nonlinear Plasmonic Cloaks to Realize Giant All-Optical Scattering Switching. *Phys. Rev. Lett.* 108, 263905. doi:10.1103/physrevlett.108.263905

Bi, L., Hu, J., Jiang, P., Kim, D. H., Dionne, G. F., Kimerling, L. C., et al. (2011). On-chip Optical Isolation in Monolithically Integrated Non-reciprocal Optical Resonators. *Nat. Photon* 5, 758–762. doi:10.1038/nphoton.2011.270

Bogdanov, A. A., Koshelev, K. L., Kapitanova, P. V., Rybin, M. V., Gladyshev, S. A., Sadrieva, Z. F., et al. (2019). Bound States in the Continuum and Fano Resonances in the strong Mode Coupling Regime. *Adv. Photon.* 1, 016001. doi:10.1117/1.ap.1.1.016001

Dabidian, N., Kholmanov, I., Khanikaev, A. B., Tatar, K., Trendafilov, S., Mousavi, S. H., et al. (2015). Electrical Switching of Infrared Light Using Graphene Integration with Plasmonic Fano Resonant Metasurfaces. *ACS Photon.* 2, 216–227. doi:10.1021/ph5003279

Dmitriev, V., Kawakatsu, M. N., and de Souza, F. J. M. (2012). Compact Three-Port Optical Two-Dimensional Photonic crystal-based Circulator of W-Format. *Opt. Lett.* 37, 3192. doi:10.1364/ol.37.003192

Fano, U. (1961). Effects of Configuration Interaction on Intensities and Phase Shifts. *Phys. Rev.* 124, 1866–1878. doi:10.1103/physrev.124.1866

Guan, G., Jiang, H., Li, H., Zhang, Y., Chen, H., and Zhu, S. (2006). Tunneling Modes of Photonic Heterostructures Consisting of Single-Negative Materials. *Appl. Phys. Lett.* 88, 211112. doi:10.1063/1.2207218

Guo, Z., Jiang, H., and Chen, H. (2022). Zero-index and Hyperbolic Metacavities: Fundamentals and Applications. *J. Phys. D: Appl. Phys.* 55, 083001. doi:10.1088/1361-6463/ac2e89

Guo, Z., Long, Y., Jiang, H., Ren, J., and Chen, H. (2021). Anomalous Unidirectional Excitation of High-K Hyperbolic Modes Using All-Electric Metasources. *Adv. Photon.* 3, 036001. doi:10.1117/1.ap.3.3.036001

Guo, Z., Wu, F., Xue, C., Jiang, H., Sun, Y., Li, Y., et al. (2018). Significant Enhancement of Magneto-Optical Effect in One-Dimensional Photonic Crystals with a Magnetized Epsilon-Near-Zero Defect. *J. Appl. Phys.* 124, 103104. doi:10.1063/1.5042096

Guo, Z., Zhang, T., Song, J., Jiang, H., and Chen, H. (2021). Sensitivity of Topological Edge States in a Non-hermitian Dimer Chain. *Photon. Res.* 9, 574. doi:10.1364/prj.413873

Gupta, M., Srivastava, Y. K., Manjappa, M., and Singh, R. (2017). Sensing with Toroidal Metamaterial. *Appl. Phys. Lett.* 110, 121108. doi:10.1063/1.4978672

Pariente, J. A., Bayat, F., Pecharomán, C., Blanco, A., García-Martín, A., and López, C., Percolation in Photonic Crystals Revealed by Fano Resonance, arXiv: 1607.08890 (2016).

Kharratian, S., Urey, H., and Onbaşlı, M. C. (2020). Advanced Materials and Device Architectures for Magnetooptical Spatial Light Modulators. *Adv. Opt. Mater.* 8, 1901381. doi:10.1002/adom.201901381

Leviyev, A., Stein, B., Christofi, A., Galfsky, T., Krishnamoorthy, H., Kuskovsky, I. L., et al. (2017). Nonreciprocity and One-Way Topological Transitions in Hyperbolic Metamaterials. *APL Photon.* 2, 076103. doi:10.1063/1.4985064

Liberal, I., and Engheta, N. (2017). Near-zero Refractive index Photonics. *Nat. Photon.* 149. doi:10.1038/nphoton.2017.13

Limonov, M. F., Rybin, M. V., Poddubny, A. N., and Kivshar, Y. S. (2017). Fano Resonances in Photonics. *Nat. Photon* 11, 543–554. doi:10.1038/nphoton.2017.142

Manjappa, M., Pitchappa, P., Singh, N., Wang, N., Zheludev, N. I., Lee, C., et al. (2018). Reconfigurable MEMS Fano Metasurfaces with Multiple-Input-Output States for Logic Operations at Terahertz Frequencies. *Nat. Commun.* 9, 4056. doi:10.1038/s41467-018-06360-5

Miroshnichenko, A. E., Flach, S., and Kivshar, Y. S. (2010). Fano Resonances in Nanoscale Structures. *Rev. Mod. Phys.* 82, 2257–2298. doi:10.1103/revmodphys.82.2257

Niu, X., Hu, X., Chu, S., and Gong, Q. (2018). Epsilon-Near-Zero Photonics: A New Platform for Integrated Devices. *Adv. Opt. Mater.* 6, 1701292. doi:10.1002/adom.201701292

Ott, C., Kaldun, A., Raith, P., Meyer, K., Laux, M., Evers, J., et al. (2013). Lorentz Meets Fano in Spectral Line Shapes: A Universal Phase and its Laser Control. *Science* 340, 716–720. doi:10.1126/science.1234407

Pham, T. S., Ranaweera, A. K., Ngo, D. V., and Lee, J.-W. (2017). Analysis and Experiments on Fano Interference Using a 2D Metamaterial Cavity for Field Localized Wireless Power Transfer. *J. Phys. D: Appl. Phys.* 50, 305102. doi:10.1088/1361-6463/aa7988

Pintus, P., Di Pasquale, F., and Bowers, J. E. (2013). Integrated TE and TM Optical Circulators on Ultra-low-loss Silicon Nitride Platform. *Opt. Express* 21, 5041. doi:10.1364/oe.21.005041

Poddubny, A. N., Rybin, M. V., Limonov, M. F., and Kivshar, Y. S. (2012). Fano Interference Governs Wave Transport in Disordered Systems. *Nat. Commun.* 3, 914. doi:10.1038/ncomms1924

Rybin, M. V., Khanikaev, A. B., Inoue, M., Samusev, K. B., Steel, M. J., Yushin, G., et al. (2009). Fano Resonance between Mie and Bragg Scattering in Photonic Crystals. *Phys. Rev. Lett.* 103, 023901. doi:10.1103/PhysRevLett.103.023901

Rybin, M. V., Mingaleev, S. F., Limonov, M. F., and Kivshar, Y. S. (2016). Purcell Effect and Lamb Shift as Interference Phenomena. *Sci. Rep.* 6, 20599. doi:10.1038/srep20599

Rybin, M. V., Samusev, K. B., Sinev, I. S., Semouchkin, G., Semouchkina, E., Kivshar, Y. S., et al. (2013). Mie Scattering as a cascade of Fano Resonances. *Opt. Express* 21, 30107. doi:10.1364/oe.21.030107

Singh, R., Cao, W., Al-Naib, I., Cong, L., Withayachumnankul, W., and Zhang, W. (2014). Ultrasensitive Terahertz Sensing with High-Q Fano Resonances in Metasurfaces. *Appl. Phys. Lett.* 105, 171101. doi:10.1063/1.4895595

Smigaj, W., Romero-Vivas, J., Gralak, B., Magdenko, L., Dagens, B., and Vanwolleghem, M. (2010). Magneto-optical Circulator Designed for Operation in a Uniform External Magnetic Field. *Opt. Lett.* 35, 568–570. doi:10.1364/OL.35.000568

Sounas, D. L., Caloz, C., and Alù, A. (2013). Giant Non-reciprocity at the Subwavelength Scale Using Angular Momentum-Biased Metamaterials. *Nat. Commun.* 4, 2407. doi:10.1038/ncomms3407

Takeda, H., and John, S. (2008). Compact Optical One-Way Waveguide Isolators for Photonic-Band-gap Microchips. *Phys. Rev. A.* 78, 023804. doi:10.1103/physreva.78.023804

Tan, T. C. W., Plum, E., and Singh, R. (2020). Lattice-Enhanced Fano Resonances from Bound States in the Continuum Metasurfaces. *Adv. Opt. Mater.* 8, 1901572. doi:10.1002/adom.201901572

Tribelsky, M. I., and Miroshnichenko, A. E. (2016). Giant In-Particle Field Concentration and Fano Resonances at Light Scattering by High-Refractive index Particles. *Phys. Rev. A. 93* 053837. doi:10.1103/physreva.93.053837

Tuz, V. R. (2016). Polaritons Dispersion in a Composite Ferrite-Semiconductor Structure Near Gyrotropic-Nihility State. *J. Magnetism Magn. Mater.* 419, 559–565. doi:10.1016/j.jmmm.2016.06.070

Vlasov, Y. A., Bo, X.-Z., Sturm, J. C., and Norris, D. J. (2001). On-chip Natural Assembly of Silicon Photonic Bandgap Crystals. *Nature* 414, 289–293. doi:10.1038/35104529

Wu, C., Khanikaev, A. B., Adato, R., Arju, N., Yanik, A. A., Altug, H., et al. (2012). Fano-resonant Asymmetric Metamaterials for Ultrasensitive Spectroscopy and Identification of Molecular Monolayers. *Nat. Mater* 11, 69–75. doi:10.1038/nmat3161

Wu, C., Khanikaev, A. B., and Shvets, G. (2011). Broadband Slow Light Metamaterial Based on a Double-Continuum Fano Resonance. *Phys. Rev. Lett.* 106, 107403. doi:10.1103/physrevlett.106.107403

Yanik, A. A., Cetin, A. E., Huang, M., Artar, A., Mousavi, S. H., Khanikaev, A., et al. (2011). Seeing Protein Monolayers with Naked Eye through Plasmonic Fano Resonances. *Proc. Natl. Acad. Sci.* 108, 11784–11789. doi:10.1073/pnas.1101910108

Yu, Y., Sakanas, A., Zali, A. R., Semenova, E., Yvind, K., and Mørk, J. (2021). Ultra-coherent Fano Laser Based on a Bound State in the Continuum. *Nat. Photon.* 15, 758–764. doi:10.1038/s41566-021-00860-5

Yu, Z., Veronis, G., Wang, Z., and Fan, S. (2008). One-Way Electromagnetic Waveguide Formed at the Interface between a Plasmonic Metal under a Static Magnetic Field and a Photonic crystal. *Phys. Rev. Lett.* 100, 023902. doi:10.1103/PhysRevLett.100.023902

Zangeneh-Nejad, F., and Fleury, R. (2019). Topological Fano Resonances. *Phys. Rev. Lett.* 122, 014301. doi:10.1103/PhysRevLett.122.014301

Zhang, G., Zhang, Z., Xu, Y., and Wang, J. (2018). High Speed Magneto-Optical Imaging System to Investigate Motion Characteristics of Arc

Plasma in Enclosed Chamber. *Opt. Express* 26, 23156. doi:10.1364/oe.26.023156

Zhang, Y., Du, Q., Wang, C., Fakhrul, T., Liu, S., Deng, L., et al. (2019). Monolithic Integration of Broadband Optical Isolators for Polarization-Diverse Silicon Photonics. *Optica* 6, 473. doi:10.1364/optica.6.000473

Zhang, Z.-f., Xue, C.-h., Jiang, H.-t., Lu, H., Li, Y.-h., and Chen, H. (2013). The Fano-type Transmission and Field Enhancement in Heterostructures Composed of Epsilon-Near-Zero Materials and Truncated Photonic Crystals. *Appl. Phys. Lett.* 103, 201902. doi:10.1063/1.4829858

Conflict of Interest: The authors declare that the research was conducted in the absence of any commercial or financial relationships that could be construed as a potential conflict of interest.

Publisher's Note: All claims expressed in this article are solely those of the authors and do not necessarily represent those of their affiliated organizations, or those of the publisher, the editors, and the reviewers. Any product that may be evaluated in this article, or claim that may be made by its manufacturer, is not guaranteed or endorsed by the publisher.